Charge Transport Phenomena in Heterojunction Photocatalysts: the WO_3/ TiO_2 System as an Archetypical Model

Asif Iqbal,[*,†] Andreas Kafizas,[*,‡,¶] Carlos Sotelo-Vazquez,[§] Rachel Wilson,[§] Min Ling,[§] Alaric Taylor,[‖] Chris Blackman,[§] Kirk Bevan,[†] Ivan Parkin,[§] and Raul Quesada-Cabrera[*,§]

†*Materials Engineering, McGill University, 3610 University Street, Montréal QC H3A 0C5, Canada.*

‡*Department of Chemistry, Imperial College London, London SW7 2AZ, United Kingdom.*

¶*The Grantham Institute, Imperial College London, London SW7 2AZ, United Kingdom.*

§*Department of Chemistry, University College London, 20 Gordon Street, London WC1H 0AJ, United Kingdom.*

‖*Department of Electronic & Electrical Engineering, University College London, Torrington Place, London WC1E 7JE, United Kingdom.*

E-mail: asif.iqbal@mail.mcgill.ca; a.kafizas@imperial.ac.uk; r.quesada@ucl.ac.uk

Abstract

Recent studies have demonstrated the high efficiency through which nanostructured core-shell WO_3/TiO_2 (WT) heterojunctions can photocatalytically degrade model organic pollutants (stearic acid, QE $\sim$ 18% @ λ = 365 nm), and as such, has varied potential environmental and antimicrobial applications. The key motivation herein is to connect theoretical calculations of charge transport phenomena, with experimental

measures of charge carrier behaviour using transient absorption spectroscopy (TAS), to develop a fundamental understanding of how such WT heterojunctions achieve high photocatalytic efficiency (in comparison to standalone WO_3 and TiO_2 photocatalysts). This work reveals an order of magnitude enhancement in electron and hole recombination lifetimes, respectively located in the TiO_2 and WO_3 sides, when an optimally designed WT heterojunction photocatalyst operates under UV excitation. This observation is further supported by our computationally captured details of conduction band and valence band processes, identified as: (i) dominant electron transfer from WO_3 to TiO_2 *via* the diffusion of excess electrons; and (ii) dominant hole transfer from TiO_2 to WO_3 *via* thermionic emission over the valence band edge. Simultaneously, our combined theoretical and experimental study offers a time-resolved understanding of what occurs on the micro- to milli-seconds (μs–ms) timescale in this archetypical photocatalytic heterojunction. At the microsecond timescale, a portion of the accumulated holes in WO_3 contribute to the depopulation of W^{5+} polaronic states, while remaining accumulated holes in WO_3 are separated from adjacent electrons in TiO_2 up to 3 ms after photoexcitation. The presence of these exceptionally long-lived photogenerated carriers, dynamically separated by the WT heterojunction, is the origin of the superior photocatalytic efficiency displayed by this system (in the degradation of stearic acid). Consequently, our combined computational and experimental approach delivers a robust understanding of the direction of charge separation along with critical time-resolved insights into the evolution of charge transport phenomena in this model heterojunction photocatalyst.

Keywords

Heterojunction Photocatalyst, Charge Transport, Metal Oxide Semiconductors, WO_3/TiO_2.

1 Introduction

In recent times, heterojunctions have emerged as a proven strategy to engineer the charge transport properties of photoactive semiconducting materials.[1–3] The formation of a semiconductor heterojunction comes with the advantage of modifying the landscape of carrier transport processes including, but not limited to, the efficient separation of photogenerated carriers,[4,5] suppression of minority carrier recombination,[6,7] efficient carrier extraction when used alongside dedicated electron and hole blocking layers,[8] the formation of electron and hole potential notches and highly mobile 2D carrier transport channel.[9–12] By carefully selecting the constituent materials, doping concentrations and device geometry, semiconductor heterojunctions have results in numerous advances in solid-state devices,[13,14] organic solar cells,[3,15] sensing technology,[16,17] electrochemistry and catalysis.[18–21] In line with this exciting scope, the family of transition metal oxide semiconductors (*e.g.*, TiO_2, WO_3, α-Fe_2O_3, $BiVO_4$) arranged within conventional type-II, Z-scheme and S-scheme heterostructures has drawn intensive attention in the literature.[18–29] This strategy of formation of heterojunction photocatalyst has already demonstrated considerable improvement in photo(electro)chemical performance compared to those of the individual materials-based monolithic photoelectrodes, with notable examples being as WO_3/TiO_2,[21–23] $ZnO/BiVO_4$,[24] Cu_2O/TiO_2,[30] rutile/anatase[31–35] and more recently, $WO_3/BiVO_4$.[7,18–20]

Though many research reports have attributed the performance enhancement of semiconductor heterojunctions to a synergetic interaction between the two light-absorbing materials, a clear picture of the charge transport processes that take place remains largely elusive.[7,18–21,32] By creating a heterojunction, the new geometry of the photoactive device offers new pathways for carrier transport, making it complex to determine the fate of photogenerated electrons and holes during photocatalysis. The widely used picture of static band alignment diagrams,[26] with flat band energies at the junction, can be highly misleading and does not provide concrete insight into the charge transport processes that occur at such heterojunctions. A static band alignment only partially depicts the electronic landscape of

heterojunction materials, and thus it should be treated with care. This limitation depicts the urgent need for comprehensive computations capturing the charge transport processes in a heterojunction photocatalyst and has spurred a recent surge in multiscale computational research.[36–38] There is also a significant amount of experimental research that extracted or suggested the direction of charge flow for a large list of heterojunction photocatalysts, such as $WO_3/BiVO_4$,[7,18–20] WO_3/Sb_2S_3,[39] TiO_2/CdS,[40,41] $TiO_2/CsPbBr_3$,[42] ZnO/Cu_xO[43] to name a few. However, numerous scientific investigations have reported contradictory directions of charge flow for a given pair of materials. Rutile/anatase[32–35] and WO_3/TiO_2[21–23] systems are a few of the notable examples investigated in this regard. Additionally, the presence of distributed trap states (such as polaronic states, bulk defect states) can impact substantially upon carrier flow.[32,44,45] Likewise, it is important to consider the geometry of a heterojunction along with its light penetration and absorption profiles. Therefore, comprehensive theoretical and experimental studies are necessary to unravel the intricate processes and details of charge dynamics in heterojunction photocatalyst systems.

In the current work, the full landscape of charge transport phenomena within a semiconductor heterojunction is considered using the WO_3/TiO_2 (WT) system as an archetypical model. Our study is motivated by record-efficiency nanostructured WT coatings for the degradation of a model organic pollutant (stearic acid, QE $\sim 18\%$ @ $\lambda = 365$ nm), recently reported by some of the co-authors.[21] However, the methodology developed herein can (and should) be applied to many promising heterojunctions for applications in photocatalysis, including solar-to-chemical energy conversion and environmental systems. As in many notable heterojunctions explored to date, contradictory observations have been found in WT. No consensus has been reached to explain the electronic behavior and charge transport processes in this system.[21–23] Moreover, the similar absorption properties of photogenerated electrons and holes in WO_3 and TiO_2 makes it a challenging system to ascertain the direction of charge transfer through the junction using transient absorption spectroscopy.[21] In this regard, the combined theoretical and experimental approach developed herein shows that under UV illu-

mination an optimally designed core-shell WT junction preferentially allows photogenerated holes to transfer to the WO_3 side. Once the photogenerated holes move to WO_3, they are found to stay in WO_3 as a large energy barrier in the valence band prevents their transfer to the TiO_2 side. Additionally, the photogenerated electrons in WO_3 transfer to the TiO_2 side *via* a conduction band electron diffusion process influenced by band-flattening due to the generation of a photovoltage. Consequently, our numerical computations and experimental transient absorption spectroscopy measurements reveal that the depopulation of electrons in W^{5+} polaronic states by photogenerated holes in the WT junction happens at a timescale $\sim$20 μs after the UV illumination. Thus, we find this depopulation process becomes significantly delayed (by orders of magnitude) compared to similar processes occurring within 100-200 ps in standalone WO_3 photocatalysts. Finally, this study shows that an optimally designed WT junction simultaneously allows long-lived holes in WO_3 and electrons in TiO_2 sides and is able to separate these carriers up to a timescale of $\sim$3 ms. These exceptionally long carrier lifetimes (for metal oxides) ultimately results in the record-efficiency nanostructured WT coating for the degradation of stearic acid (as recently reported by some of the co-authors).[21]

2 Methods

2.1 Synthesis and Physical Characterization

Nanostructured, rod-like WO_3 films were deposited on quartz slides from a 2:1 mixture of acetone (99%) and methanol (99.5%) dispersion (15 ml) of tungsten hexacarbonyl ($W(CO)_6$, 0.060 g, 99%), using aerosol-assisted CVD and following a procedure described elsewhere.[46] These WO_3 rods were conformally coated with TiO_2 thin films using atomic layer deposition (ALD). Fig. 1a-b shows schematics of the WO_3/TiO_2 (WT) coating and a single nanorod WT heterojunction, respectively, considered in this study. The radius of the WO_3 nanorod (L_W) was on average $\sim$30 nm, whereas the thickness of TiO_2 film (L_T) was varied by control-

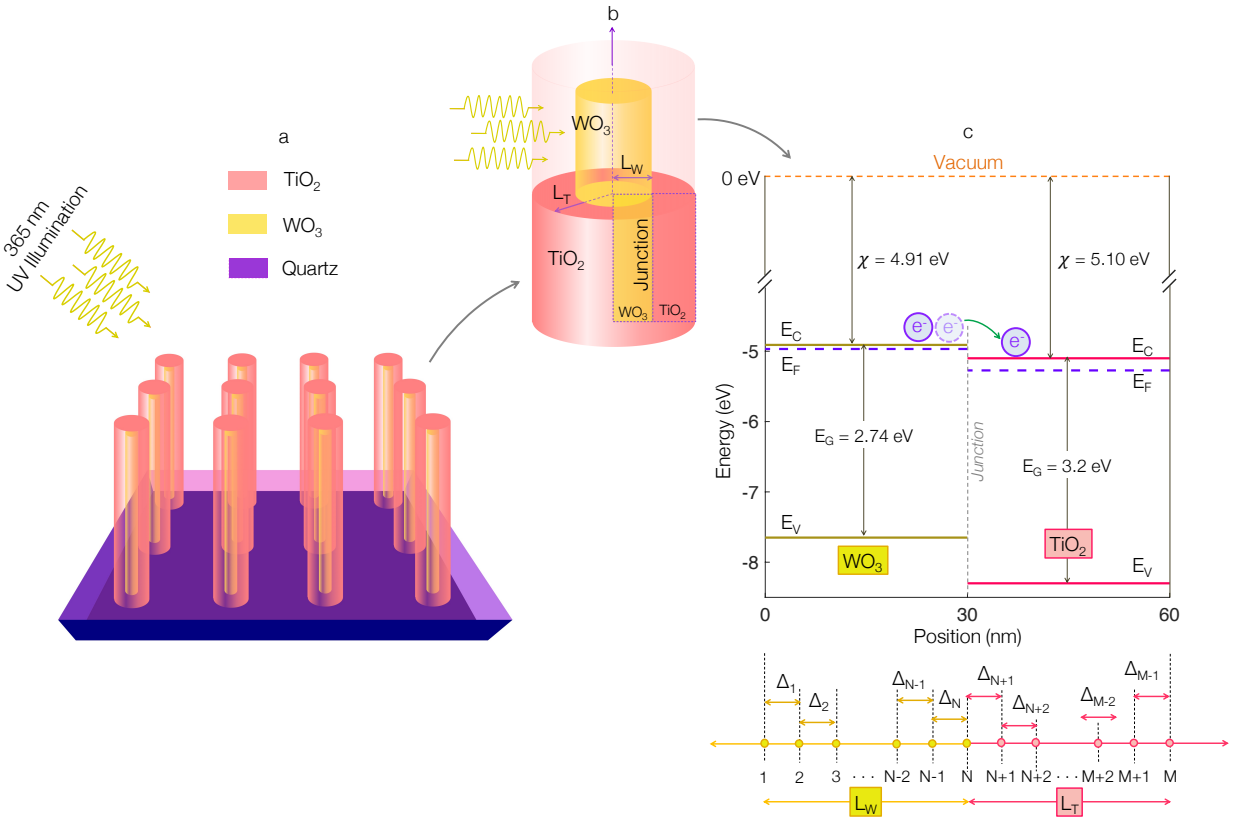

Figure 1: A schematic illustration of the WO_3/TiO_2 (WT) heterojunction photocatalyst under consideration in this work is exhibited in part (a). As can be seen, TiO_2 is conformally deposited using ALD on aligned WO_3 nanorods, grown on quartz substrate using CVD, to construct the photoactive heterojunction, which is excited by 365 nm UV illumination. Part (b) shows a close-up view of a single WT junction with an illustration of the geometry of the photocatalyst. Here, L_W and L_T represent the radius of the WO_3 nanorod and thickness of TiO_2 coating, respectively and the physical location of the junction is also given. Part (c) demonstrates the relative positions of the energy band diagrams of WO_3 and TiO_2 with vacuum level as the reference energy level (0 eV). For better understanding, the critical material parameters, *e.g.*, bandgaps (E_G), electron affinity levels (χ) are also shown. The illustration at the bottom shows how the 1D spatial dimension (x - grid) is non-uniformly discretized into grid points separated by Δ_i, where, i = [1, 2, ... ,N-1, N, N+1, ... , M]. Here, i = N is the physical location of the heterojunction and i = M marks the outer surface of TiO_2 layer.

ling the number of ALD cycles. deposition time by ALD. For photocatalytic testing, the WT photocatalysts are radially photoexcited under UV light, $\lambda = 365$ nm, with irradiance (I_{uv}) of 3.15 mW cm^{-2}.

The optical properties of the WT films were evaluated using a Perkin Elmer Lambda 950 UV/Vis/NIR Spectrophotometer, calibrated using a Labsphere reflectance standard. The structural properties were investigated using X-ray diffraction (XRD) and Raman spectroscopy. XRD measurements were carried out using a Bruker-Axs D8 (Lynxeye XE) diffractometer, which consists of a monochromated Cu X-ray source ($K_{\alpha 1}$, 1.5406 Å) and a glancing incident angle (θ) of 1°. Raman spectroscopy was performed using a Renishaw 1000 spectrometer equipped with a 633 nm laser, calibrated using a silicon reference. Two different scanning electron microscopy (SEM) systems, a JEOL 6301 (5 kV) and a JEOL JSM-6700F field emission instruments, were used to explore the microstructural properties of the WT films. Transmission electron microscopy (TEM) was performed using a high resolution TEM instrument, JEOL 2100, with a LaB_6 source operating at an acceleration voltage of 200 kV. A Gatan Orius charge-coupled device (CCD) was used to obtain the sample micrographs in the TEM system. The TEM studies on single WT rods were prepared by scraping the nanorods from the quartz substrate using a diamond tipped pen, followed by sonication in methanol and drop-casting onto a 400 Cu mesh lacy carbon film grid (Agar Scientific Ltd). Energy-dispersive X-ray spectroscopy (EDS) analysis was carried out using a JEOL JSM-6700F and secondary electron image on a Hitachi S-3400 field emission instruments (20 kV) and the Oxford software INCA. X-ray photoelectron spectroscopy (XPS) was carried out in a Thermo K-Alpha spectrometer with monochromated Al K-Alpha radiation, using a dual beam charge compensation system and constant pass energy of 50 eV. A binding energy range of 0 - 1200 eV was used to collect survey scans. The main peaks of the individual elements in the WT films, Ti (2p), W (4f), O (1s) and C (1s), were obtained at high resolution. CasaXPS software was used to model the peak areas from high-resolution scans, using relative sensitive factors, to determine composition and oxidation state within the analysis

region (spot size, 400 μm). The XPS peaks were calibrated to adventitious carbon at the binding energy (B.E.) of 284.4 eV.

2.2 Transient Absorption Spectroscopy

Transient Absorption Spectroscopy (TAS) was carried out on the microsecond to second timescale (μs$\rightarrow$s) to measure the recombination kinetics of charge carriers that form in WO_3, TiO_2 and WT heterojunction films. Spectra were recorded over the wavelength range of 550 - 950 nm. A Nd:YAG laser (OPOTEK Opolette 365 II, $\sim$ 6 ns pulse width) was used as the excitation source, generating 365 nm UV light from the third harmonic. The laser light was transmitted to the WT samples *via* a fiber optic light guide. The laser was emitted with a repetition rate of 0.65 Hz at a power of $\sim$1.2 mJ cm^{-2}. The probe pulse was generated from quartz halogen lamp (a 100 W Bentham IL1). Due to the nanostructured topography of the samples, light was scattered strongly, and samples were thus measured in diffuse reflection mode. As photo-induced changes in reflectance are low ($< 1\%$), it was assumed that the transient signal was directly proportional to the concentration of excited species. The transient changes in diffuse reflectance from the WT samples were collected by a 2" diameter and 2" focal length lens and relayed to a monochromator (Oriel Cornerstone 130). Time-resolved intensity data was collected with a silicon photodiode (Hamamatsu S3071). Data at a time faster than 3.6 ms was recorded by an oscilloscope (Tektronics DPO3012) after passing through an amplifier box (Costronics), whereas data slower than 3.6 ms was simultaneously recorded on a National Instrument DAQ card (NI USB-6251). Each kinetic trace was obtained from the average of 100 to 250 laser pulses and the acquisitions were triggered by a photodiode (Thorlabs DET10A) exposed to laser scatter. A home-built LabVIEW software application was used to process data.

2.3 Theoretical Approach

A custom-made finite-difference (FD) numerical model was developed in order to discern charge transport and electrostatic properties within the WT heterojunction.[47] This model self-consistently solves the coupled Poisson-continuity equations (Eqs. 1-3):

$$\epsilon \frac{d^2\phi}{dx^2} + \frac{d\phi}{dx}\frac{d\epsilon}{dx} = -\left[Q_W + Q_T\right], \tag{1}$$

$$\frac{1}{q}\frac{dJ_n}{dx} + G_n - R_n = \frac{\partial n}{\partial t} = 0, \tag{2}$$

$$-\frac{1}{q}\frac{dJ_p}{dx} + G_p - R_p = \frac{\partial p}{\partial t} = 0. \tag{3}$$

Here, ϕ represents the electrostatic potential of the WT junction; Q_W and Q_T respectively refer to the charge densities in WO_3 and TiO_2 ('dark' and 'light' subscripts will be used to represent charges at dark and illumination conditions); J_n and J_p are the electron and hole currents, respectively; and n and p represent the spatial concentrations of electrons and holes, respectively. Electron and hole generation contributions are given by G_n and G_p and can be computed *via* the Lambert-Beer law. Similarly, R_n and R_p refer to trap-assisted Shockley-Read-Hall recombination for electrons and holes, respectively. Other parameters include the spatial/material dependence of the dielectric constant ϵ and grid discretization along x. A list of all parameters related to the WT heterojunction is given in Table S1 in SI. In order to replicate the experimental procedures (*e.g.*, photovoltage generation and band bending), appropriate boundary conditions were applied during the solution of Eqs. 1-3, as detailed elsewhere.[47–49] In our numerical simulation of WT junctions, the solutions of the coupled semiclassical transport equations (Eqs. 1-3) were sought in a linearly discretized x - grid. Fig. 1c presents the discretized version of the same space vector ($\vec{x}$) as shown in Fig. 1b. All the critical points along the x-grid are also shown for convenience. Within this generic implementation scheme, non-uniform spacing of the grid points was utilized. Here, Δ_i represents the spacing between two consecutive grid points i and $i+1$, where i can be

any value from [1 : M-1]. Grid points [1 : N] were located in WO_3, while grid points [N+1 : M] were placed in the TiO_2 and i = N marked the physical location of the heterojunction. Discretizing the x-grid in a non-uniform fashion comes with the advantages of fast and efficient computation albeit with the cost of complexity in the numerical formulation.[50] The numerical details are discussed in earlier studies by some of the co-authors.[47–49]

3 Results and Discussion

3.1 Electrostatics and Charge Transport Properties

3.1.1 Energy Band Diagrams Under Dark and UV Light

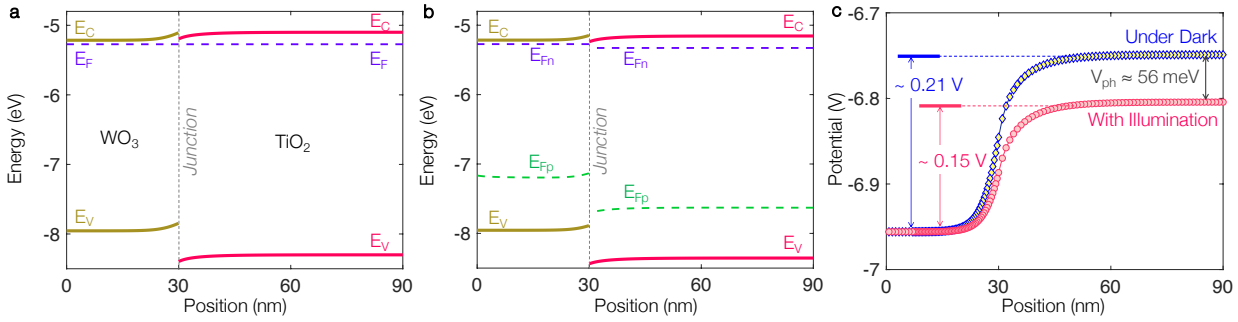

Figure 2: Calculated energy band diagrams of WO_3/TiO_2 heterojunction photocatalyst under dark (a) and UV illumination (b). Here, we considered $L_W = 30$ nm and $L_T = 60$ nm. In addition, we assumed the vacuum level energy in the bulk of TiO_2 (under dark condition) as the reference potential (0 eV) to compute the band diagrams. The computed energy band diagram at equilibrium clearly show a constant Fermi level, a large potential barrier for holes in WO_3 (forming a 'hole-notch'), a small potential barrier for electrons in TiO_2 (forming an 'electron-notch') and discontinuities in conduction and valence bands at the junction – all the characteristics of an abrupt isotype heterojunction.[9–11,51] Under performance with light, the junction exhibits the generation of a small photovoltage (V_{ph}) and the splitting of electron and hole quasi-Fermi levels. Part (c) presents the spatial distributions of electrostatic potential at equilibrium (V_{dark} marked by yellow squares) and under illumination (V_{light} marked by red circles). A V_{ph} of 60 meV is estimated by comparing V_{dark} and V_{light}, which acts similar to an applied forward bias by reducing the band bending of the junction.

Figs. 2–3 present the results from our numerical computation of the electrostatics and charge transport properties of the WO_3/TiO_2 heterojunction. Throughout our computa-

tional analysis, special attention was given to use the material parameters that were reported in the literature (Table S1 in SI outlines the values used in our simulation along with the relevant references). Both TiO_2 and WO_3 are inherently n-type in character.[21,33,52,53] Therefore, the WT heterojunction appears to be an abrupt 'n-n' isotype heterojunction, treating electrons and holes as majority and minority carriers, respectively.[11] Fig. 1c presents the band alignment of the WT heterojunction prior to the equilibration of the Fermi levels in the system.[33] It is imperative to understand that a static band alignment sketch of this kind can only depict the preferential movement of the carriers until the initial equilibration condition is accomplished (otherwise known as the 'dark equilibrium' condition of the heterojunction).[11] In a generic description, the force that selectively driving carrier transport under operating conditions is solely determined by the relative positions of the Fermi levels on both sides of a semiconductor heterojunction. For example, in this WT junction, when a contact is made between WO_3 and TiO_2 (creating an n-n heterojunction) electrons from the WO_3 preferentially transfer to the TiO_2 side to establish a constant Fermi level (E_F). This electron transfer is illustrated in Fig. 1c. Under equilibrium, this flat Fermi level determines the concentrations of conduction band (CB) electrons (n_{dark}) and valence band (VB) holes (p_{dark}) in both WO_3 and TiO_2.

Fig. 2a presents our computed equilibrium band diagram of the WT heterojunction. Here, we considered $L_W = 30$ nm and $L_T = 60$ nm. Under equilibrium a flat E_F is present throughout the entire system, indicating net zero current flow ($J = 0$). In addition, a space charge region (SCR_{dark}) is formed due to the transfer of electrons from WO_3 to TiO_2. The details of SCR_{dark} will be discussed later in Section 3.1.2 (*vide infra*). When the WT heterojunction is brought under 365 nm UV illumination, photogenerated electron-hole pairs are created and a photovoltage (V_{ph}) developes. Fig. 2b presents the band diagram of the WT junction under UV illumination. The impact of UV illumination on our computed band diagram picture is two-fold: (i) the splitting of electron and hole Fermi levels into the corresponding quasi-Fermi levels (represented by E_{Fn} for electron and E_{Fp} for hole, respec-

tively); and (ii) the process of band-flattening due to the generation of a photovoltage.[47,54] For clarity, Fig. 2c depicts the electrostatic potentials both under dark (V_{dark}) and illumination (V_{light}). By comparing both of these spatial distributions of the electrostatic potential, an estimated band-flattening of 60 meV is caused by UV illumination.

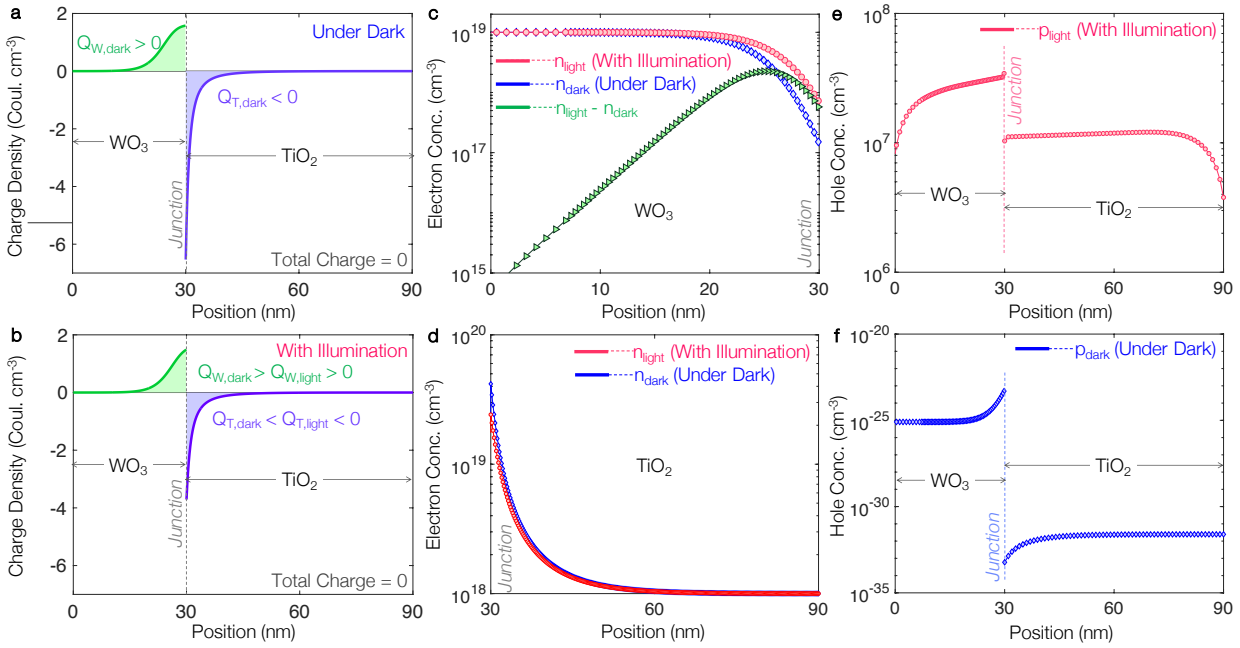

Figure 3: Calculated distributions of net charge densities under equilibrium (a) and illuminated (b) conditions, also known as the respective charge densities in the space charge regions (SCR_{dark} and SCR_{light}). Under equilibrium, WO_3 exhibits a net positive charge and TiO_2 exhibits a net negative charge. This is due to the junction's effort to make a flat Fermi level by transferring electrons from WO_3 side to TiO_2 side. The extent of the space charge region is reduced when the junction is exposed to UV illumination. This can be comprehended as the weakening of the electric field due to the band-flattening process brought about by the illumination. The ultimate impact of this coupled electrostatic and charge transport process is the presence of the excess electrons in WO_3 side, as shown in part (c) in green triangles and computed as the difference between electron concentrations under illuminations (n_{light}, marked by red circles) and dark conditions (n_{dark}, marked by blue squares). (d) Calculated distributions of electron concentration in TiO_2 under illuminations (n_{light}, marked by red circles) and dark conditions (n_{dark}, marked by blue squares). Calculated distributions of hole concentration along the WT junction under illumination and dark conditions are respectively shown in part (e) and part (f).

3.1.2 Charge Distributions Under Dark and UV Light

To delve more into the electrostatic and charge transport properties of the WT junction ($L_W = 30$ nm; $L_T = 60$ nm), the evolution of net charge distributions ($Q_W + Q_T$) was studied along with the space vector $\vec{x}$. Figs. 3a-b exhibit the charge density distributions under both dark and UV illumination. As can be seen, without illumination (dark, equilibrium condition) the WO_3 side shows a net positive charge accumulation ($Q_{W,dark}$), whereas the TiO_2 side contains a net negative depletion charge ($Q_{T,dark}$). This is a direct consequence of a net electron transport from WO_3 into TiO_2 upon creation of the WT heterojunction. However, the net total charge of the junction always remains zero ($Q_{W,dark} + Q_{T,dark} = 0$) and thus the junction maintains the fundamental law of charge conservation.

Upon illumination, a degree of *band-flattening* takes place due to an equal amount of photovoltage generation (Fig. 2c). This photovoltage works similar to an externally applied forward potential across the junction, and reduces the overall band bending (hence, this process is often referred as 'band-flattening').[47] The generated photovoltage, albeit very small, acts as a forward bias that lowers the barrier for majority carrier (electron) transport and reduces the strength of the space charge region SCR_{dark} to SCR_{light}. As can be seen from Fig. 3b, the net positive charge in the WO_3 side of the junction under illumination ($Q_{W,light}$) is reduced compared to its value under dark ($Q_{W,dark}$) as the electron concentration in WO_3 increases due the band-flattening process. Conversely, the net negative charge in TiO_2 under illumination ($Q_{T,light}$) also reduces compared to its value under dark ($Q_{T,dark}$). Fig. 3c shows calculations of the electron concentrations in the WO_3 side of the junction under dark (marked in blue squares) and UV illumination (marked in red circles). Comparison between these two computational insights reveals the generation of excess photogenerated electrons (marked in green triangles) located in WO_3, which accumulate near the junction. In addition, we find the concentration of electrons in the TiO_2 side is reduced when the junction is exposed to UV illumination (see Fig. 3d) as the electron quasi-Fermi level moves further away from the conduction band minimum in TiO_2 (captured in the calculation presented in

Fig. 2b). We also computed the concentration of holes with and without UV illumination, respectively shown in Fig. 3e and Fig. 3f. As expected, being inherently n-type semiconductors, the hole population in both WO_3 and TiO_2 is negligible in the dark. Nevertheless, a large number of holes are generated throughout the WT junction during illumination, where the WO_3 side demonstrates a higher amount of hole accumulation.

3.2 Conduction Band Processes

Fig. 4 illustrates a generic scheme for both dark equilibrium and under UV illumination charge transports for the WT heterojunction (L_W = 30 nm; L_T = 60 nm). The band theory of solid semiconductors allows for the transfer of electrons and holes *via* drift, diffusion, tunneling and thermionic emission processes.[11] Considering the conduction band (CB) process of electron transfer at dark equilibrium, the electron drift current *via* the conduction band is given by Eq. 4:[50]

$$J_{n,drift} = -qn\mu_n\vec{E}_{field}, \tag{4}$$

driven by the electric field ($\vec{E}_{field}$), which preferentially drives electron motion in the opposite direction of ($\vec{E}_{field}$).[11] Here, q denotes the charge of an electron and μ_n represents the electron mobility. Our calculations of spatially exposed charge densities (as shown in Figs. 3a-b) indicate the presence of an electric field pointing towards TiO_2. Fig. S2 shows the ($\vec{E}_{field}$) calculated in this study. Therefore, in the case of the conduction band charge transport process, the drift component of electron current implies electrons transfer from TiO_2 to WO_3 ($J_{n,T\rightarrow W}$). However, due to the discontinuity of the conduction bands between TiO_2 and WO_3, electron transfer from TiO_2 to WO_3 is impeded by a considerably small potential barrier of 90 meV (which, as shown in Fig. 4a-b, remains unaltered under UV illumination and is given by the discontinuity in the conductions band edges at the junction).

Conversely, the diffusion component of the electron current is driven by the electron

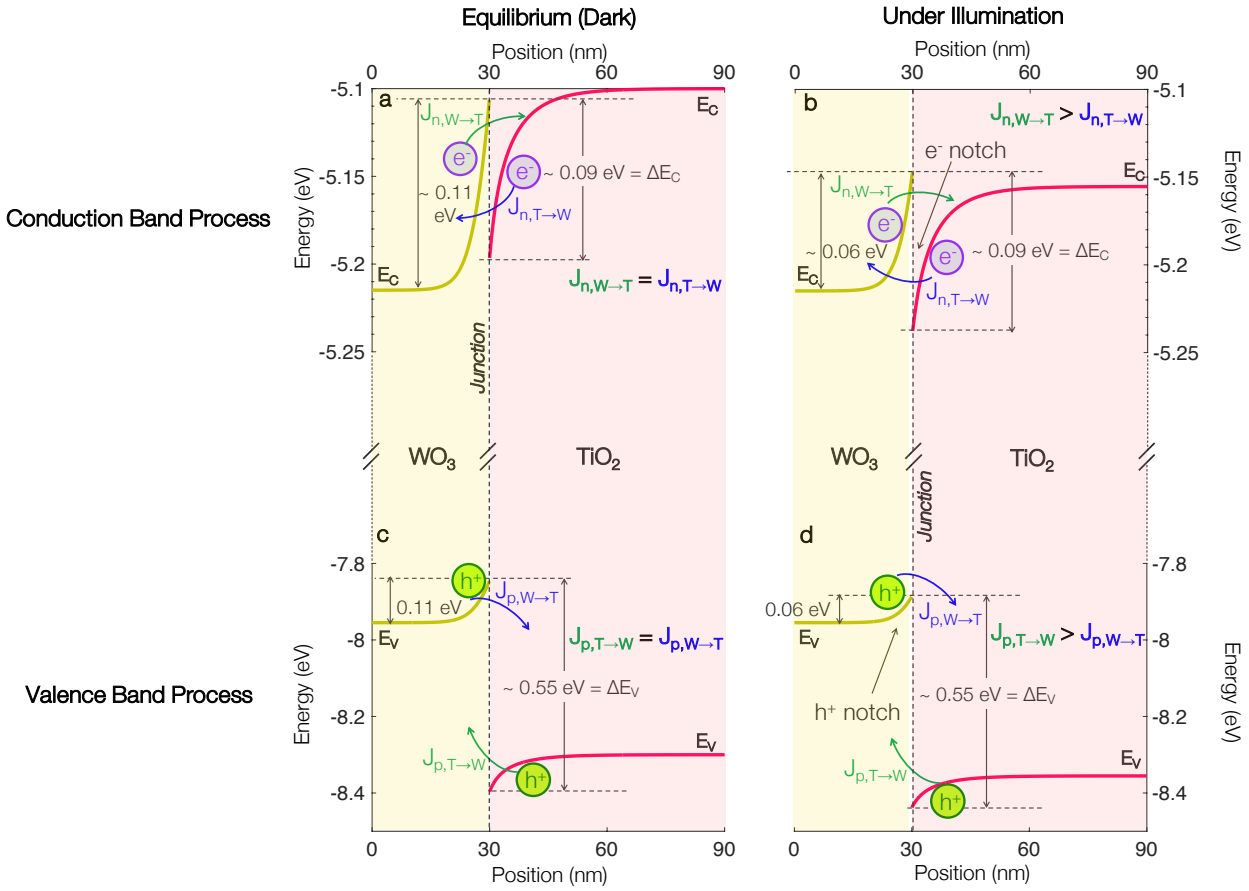

Figure 4: An illustration of various charge transfer processes at the WT junction ($L_W = 30$ nm, $L_T = 60$ nm) under dark equilibrium (left) and UV illumination (right). Our calculations of energy band diagrams for the same operating conditions of the WT junction are also presented here. For the conduction band processes, under equilibrium condition (a: top left), electron transfer from WO_3 to TiO_2 ($J_{n,W\to T}$), diffusion component of electron currents) is balanced by the counter electron transfer from TiO_2 to WO_3 ($J_{p,T\to W}$, drift component of electron currents), whereas the thermionic emission of electrons in conduction band is negligible. The conduction band experiences band-flattening when the junction is exposed to UV illumination (b: top right) and the electron transfer from WO_3 to TiO_2 increases as the potential barrier in WO_3 is reduced by ∼50 meV. Consequently, the heterojunction exhibits a net electron transfer from WO_3 to TiO_2 under UV illumination. Likewise, the components of hole currents *via* the valence band under equilibrium are balanced (c: bottom left). However, in this case, the drift component and diffusion component of hole currents are negligible due to holes being the minority carrier (see also Fig. 3f). In addition, thermionic emission of holes over the barrier is the dominant mechanism of hole transfer. As can be seen from the valence band (bottom), the hole transfer from WO_3 to TiO_2 is impeded by a large potential barrier of ∼0.55 eV and thus the holes in the WO_3 side (generated from illumination in WO_3 or transferred from TiO_2) remain in WO_3. However, an increase in hole transfer to the WO_3 side, due to UV excitation and valence band flattening is brought about by an increase in photovoltage (d: bottom right).

concentration gradient (Eq. 5):[50]

$$J_{n,diff} = -qD_n\nabla n, \tag{5}$$

where D_n represents the electron diffusion constant. In the case of electron transport *via* conduction band, the diffusion of electron occurs from WO_3 to TiO_2 ($J_{n,W\rightarrow T}$). This is because WO_3, being the dominant n-type semiconductor of the heterojunction, contains a higher spatial density of electrons. However, this electron diffusion process is also impeded under equilibrium by an upward energy barrier of 110 meV, as shown in Fig. 4a. Under equilibrium conditions, the drift component of electron transfer is countered by the diffusion component ($J_{n,W\rightarrow T} = J_{n,T\rightarrow W}$) and the net current *via* conduction band electron transport is zero.[11] This balance in electron transport processes is depicted in Fig. 4a. The balance between drift and diffusion components is disturbed by UV illumination on the WT heterojunction (Fig. 4b). To comprehend, let us recall the accumulation of excess electrons in WO_3 as a consequence of the band-flattening process, brought about by illumination (as presented in Fig. 3c). Concurrently, our computation shows that the electrostatic barrier preventing the diffusion of electrons from WO_3 to TiO_2 is also reduced to ∼60 meV – a situation that drives electron diffusion from WO_3 to TiO_2 ($J_{n,W\rightarrow T}$).[11] In contrast, the electron drift current *via* conduction band electron transfer under illumination is slightly retarded as the strength of the electric field driving the drift current is reduced, and the electron quasi-Fermi level moves further away from the conduction band minimum in TiO_2, resulting in a reduced electron population in TiO_2. Both of these effects are captured in our calculations and exhibited in Fig. S2 (computed electric field) and Fig. 3d (electron concentration in TiO_2). As a result, under UV illumination $J_{n,diff} > J_{n,drift}$, and the WT heterojunction allows preferential electron transfer from the WO_3 side to the TiO_2 side ($J_{n,W\rightarrow T} > J_{n,T\rightarrow W}$).

Finally, it is also important to consider the thermionic emission of electrons over the conduction band barrier. Previous research on semiconductor heterojunctions (and also

metal-semiconductor contacts) attributed the thermionic emission of electrons from semiconductor 1 to semiconductor 2 as the dominant transport mechanism when the conduction band discontinuity at the interface ($\Delta E_C = E_{C_1,int} - E_{C_2,int}$) is large and $E_{C_1,int} > E_{C_2,bulk}$.[11] Here, $E_{C_1,int}$ and $E_{C_2,int}$ are the conduction band minima of semiconductors 1 and 2, respectively, at the heterojunction interface and $E_{C_2,bulk}$ is the conduction band minimum of semiconductor 2 at the neutral bulk. As can be seen from Figs. 4a-b, our computational results reveal $E_{C_W,int} \sim$ -5.11 eV, $E_{C_T,bulk} \sim$ -5.10 eV and a discontinuity in the conduction bands of 90 meV, exhibiting a small potential barrier for electron transfer (here, WO_3 and TiO_2 are considered as semiconductor 1 and 2, respectively). This, in turn, implies negligible thermionic emission of electrons. Nevertheless, due to the discontinuity in the conduction bands, the WT heterojunction forms a potential notch on the TiO_2 side. This observation is in agreement with literature reports that show potential notch formation in an isotype semiconductor heterojunction.[9–11,51,55]

3.3 Valence Band Process

Similar to the case of electron transport *via* the conduction band, hole drift and diffusion *via* the valence band are also in balance under equilibrium. Nevertheless, our computational results (Figs. 4c-d) show that the drift and diffusion hole currents are negligible in the WT heterojunction. This is a direct consequence of holes being the minority carrier in both WO_3 and TiO_2 (see the negligible hole concentrations compared to the electron concentration as computed in Figs. 3e-f), as well as the large 0.55 eV discontinuity in the valence bands (ΔE_V) that appears as a large potential barrier for hole transport from WO_3 to TiO_2 side.[11] It is worth noting that for valence band hole transport $E_{V_W,bulk} > E_{V_T,int}$, which means that the current due to hole transport is determined by the thermionic emission of holes over the barrier (ΔE_V)[11] Yet, in equilibrium, the hole transfer from TiO_2 to WO_3 ($J_{p,T\rightarrow W}$) is balanced by the hole transfer from WO_3 to TiO_2 ($J_{p,W\rightarrow T}$). The light absorption and penetration profiles (Fig. S3) show photogenerated electron-hole pairs are

generated both in WO_3 and TiO_2, and consequently, the hole population can be greatly increased under UV illumination (as seen when we compare the computations in Figs. 3e-f). We have already discussed in Section 3.2 how photogenerated electrons in WO_3 diffusively transfer to TiO_2 due to the band-flattening process. Likewise, the valence bands also exhibit an equal amount of band flattening (60 meV). Thus, the transfer of holes from TiO_2 to WO_3 ($J_{p,T\rightarrow W}$) is also increased as the concentration of photogenerated holes in TiO_2 increases, and band-flattening reduces the degree of bending in the valence bands. Conversely, hole transfers from WO_3 to TiO_2 ($J_{p,W\rightarrow T}$) remain negligible due to the presence of a large potential barrier of 0.55 eV. Therefore, the holes that are transferred from TiO_2 to WO_3 and the holes photogenerated in WO_3 effectively stay in WO_3. This is also captured in our computation of the distribution of holes in Fig. 3e.

3.4 Transient Absorption Spectroscopy

Transient absorption studies (change in absorption or ΔA) were used to explore the 'spectral' and 'temporal' behavior of excited states populated by photogenerated electrons and holes, that participate in charge transfer processes across the WT junction. The analysis of spectral features obtained from TAS measurements is related to electrons and holes populating/depopulating states in WO_3 and TiO_2, and thus can provide crucial insight into the separation of electrons and holes at a heterojunction. Moreover, the temporal nature of this method gives insight into the kinetics of recombination processes, and therefore offers information on charge carrier lifetimes and the nature of the recombination process (*e.g.*, trap-assisted recombination) *via* the characteristic decay observed.[56]

3.4.1 Spectral Analysis

Fig. 5 represents the spectral analysis from our TAS measurement on the WT junctions with $L_W = 30$ nm and a varying thickness of TiO_2 coating of $L_T = 30$ nm (Fig. 5a), $L_T = 60$ nm (Fig. 5b) and $L_T = 100$ nm (Fig. 5c). The spectral trends of the WT junction are in line with

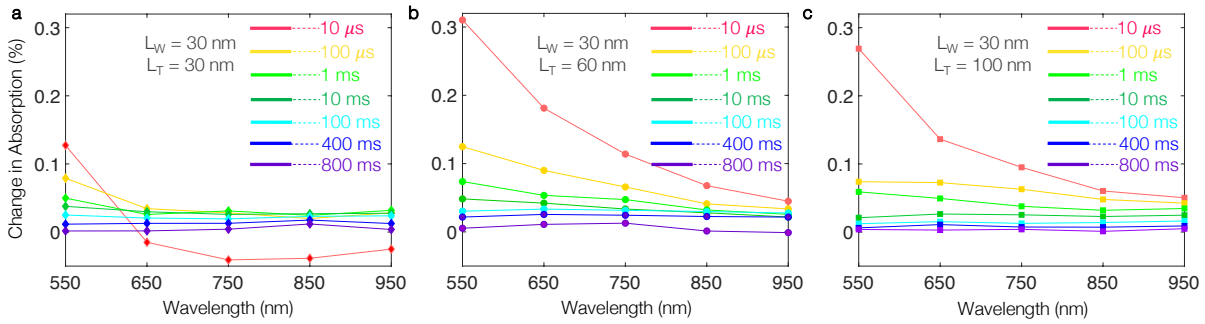

Figure 5: Transient absorption spectra (probed from 550 to 950 nm) of WT heterojunctions with L_W is 30 nm and (a) L_T = 30 nm, (b) L_T = 60 nm and (c) L_T = 100 nm. Samples were excited with a 365 nm laser pulse ($\sim$1.2 mJ cm^{-2} per pulse, 0.65 Hz pulse rate). ΔA is measured from 10 μs $\rightarrow$ 800 ms after the laser pulse excitation.

the respective spectral trends of the individual analogues.[32,52,57–59] Photogenerated electrons and holes in WO_3 absorb most strongly at $\sim$ 950 nm and $\sim$ 500 nm, respectively.[52,57] Similarly in TiO_2, electron and hole carriers absorb most strongly at $\sim$ 800 nm and $\sim$ 450 nm, respectively.[32,58] Therefore, given the similar wavelengths in which the absorption maxima occur in both semiconductors, it was not possible to distinguish the direction of charge transfer from our TAS measurements.[21] Nevertheless, we can attribute the high energy transient absorption signals (450 nm–550 nm) to highly-localized hole states and low energy transient absorption signals (650 nm–950 nm) to distributed electronic states; a tendency commonly exhibited by the family of metal oxide semiconductors and can be respectively coupled with the formations of hole and electron polarons (*e.g.*, due to oxygen vacancies).[59–61]

Fig. S4 shows the spectral features of WO_3 and TiO_2 analogues. Clearly, the formation of a WT heterojunction enhances both electron and hole signals, with a particular increase at 550 nm, which corresponds to absorption of holes.[52,57] The broad transient absorption signal due to electrons is also enhanced and situated in the infrared region. It is worth noting that the WT junction with L_T = 30 nm displays a bleach (*i.e.*, a negative transient absorption signal often caused by a loss in ground state absorption) within the 650 - 950 nm range at early timescales ($<$ 100 μs), which has previously been assigned to deep hole trapping in WO_3 to mid-gap states.[57] However, the bleach is not visible at longer timescales from 100 μs

and beyond.

3.4.2 Temporal Analysis

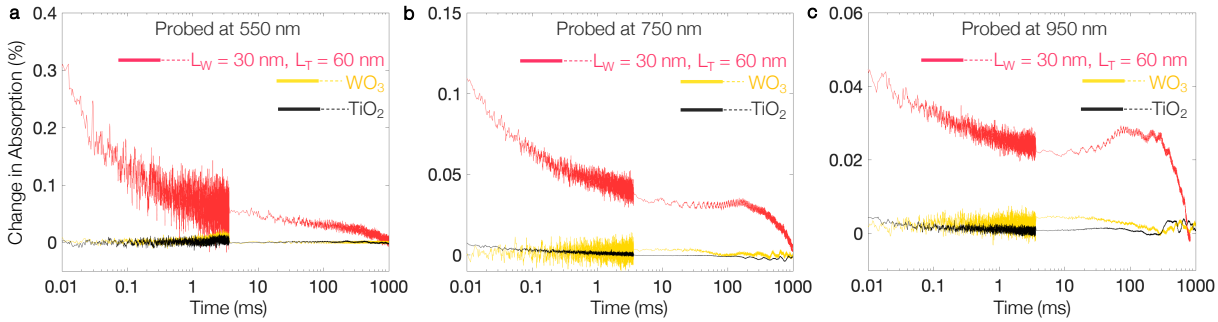

Figure 6: Transient decay dynamics at the select probe wavelengths of (a) 550 nm, (b) 750 nm and (c) 950 nm, of the WT heterojunction with $L_W = 30$ nm and $L_T = 60$ nm (marked in red). Samples were excited with a 365 nm laser pulse ($\sim$1.2 mJ cm^{-2} per pulse, 0.65 Hz pulse rate). For comparison of the improvement in charge carrier populations found in the WT junction, the traces of standalone WO_3 (marked in yellow) and TiO_2 (marked in black) are also included (see also Figs. S4-S5).

Fig. 6 shows a temporal analysis of the transient absorption process at different probe wavelengths, namely 550 nm (primarily holes), 750 nm (a mixed electron and hole signal) and 950 nm (primarily electrons) (Figs. 6a-c). The temporal features of bare WO_3 and TiO_2 samples are respectively marked in yellow and black. The WO_3 sample showed no observable difference in transient absorption over the timescales of our measurements (10 μs to 1 s), as charge carriers in WO_3 typically recombine within $\sim$200 ps[57] and are only detected at such long timescales in the presence of chemical scavengers that enhance charge carrier lifetime.[52] On the other hand, the TiO_2 sample (90 nm thick) showed weak transient absorption signals, particularly visible for the probe wavelengths 750 nm and 950 nm (see Fig. S5). The transient absorption signal follows a power law decay, indicative of trap-assisted Shockley-Read-Hall recombination and decays to the half of its initial value at $\sim$ 0.1 ms from 10 μs (Fig. S5).[56] These trends in spectral absorption and recombination dynamics are broadly consistent with previous studies of TiO_2.[58]

As can be seen in Fig. 6, compared to the individual materials, the photoexcited carriers

in the WT heterojunctions display significantly enhanced transient absorption signals for the range of probe wavelengths examined. This improvement was clearly visible for WT heterojunctions with $L_T = 30$ nm and $L_T = 60$ nm, both in terms of transient absorption and enhanced lifetime of photoexcited electrons and holes (Fig. 6). As can be seen from Fig. 6a, the change in transient absorption (ΔA) is more prominent for holes (550 nm). Transient absorption of electrons is also enhanced (750 nm and 950nm). Overall, the recombination of short-lived photogenerated carriers is substantially slowed due to junction formation between WO_3 and TiO_2. For instance, ΔA of the WT junction with a 60 nm TiO_2 coating decays to the half of its initial value at ~ 0.5 ms (from 10 μs), which is 5 times slower than TiO_2 alone.

Fig. 7 shows the transient absorption decays for WT heterojunctions with varying TiO_2 coating and probing wavelengths; Fig. 7a$\rightarrow$d: $L_T = 3$ nm $\rightarrow$ 100 nm. Interestingly, the WT junction coated with a 3 nm layer of TiO_2 shows no transient absorption signals over the timescale analyzed; similar to standalone WO_2 (see Fig. 7a and Fig. S5). However, the improvement in ΔA is clearly visible for samples with $L_T = 30$ nm (Fig. 7b), $L_T = 60$ nm (Fig. 7c) and $L_T = 100$ nm (Fig. 7d). Consequently, our TAS measurements show that the WT heterojunction can harness more photogenerated charge carriers (from the 10 μs timescale), as well as retard the kinetics of electron-hole recombination, when the thickness of the TiO_2 coating reaches a threshold of 30 nm. Moreover, this increased number of photogenerated charges and their extended lifetimes may explain the high photocatalytic activity found in WT junctions.[21]

Finally, it is also important to note from Fig. 7b that the TAS data obtained from the WT junction with $L_T = 30$ nm and probing wavelengths from 650 nm $\rightarrow$ 950 nm, display a bleaching of ΔA at early timescales (< 100 μs). A bleaching of transient absorption signal, as exhibited by a $\Delta A < 0$, represents a net depopulation of a ground state absorption. The spectral and temporal ranges of the bleaching in Figs. 5a and 7b respectively indicate that this occurs due to the depopulation of the ground state electrons in W^{5+} polaronic

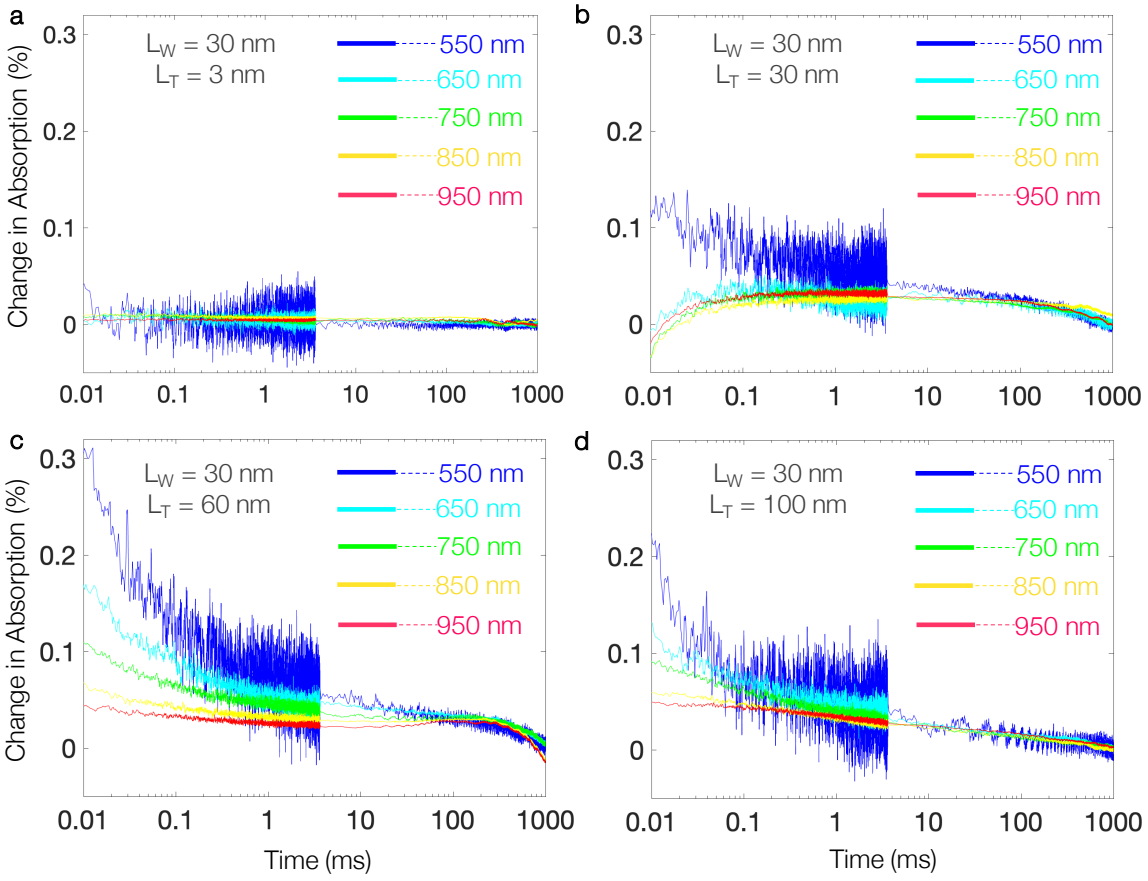

Figure 7: Transient absorption decay kinetics probed at various wavelengths (550 nm $\rightarrow$ 950 nm) for the WT heterojunctions with L_W = 30 nm and (a) L_T = 3 nm (b) L_T = 30 nm, (c) L_T = 60 nm and (d) L_T = 100 nm. Samples were excited with a 365 nm laser pulse ($\sim$1.2 mJ cm^{-2} per pulse, 0.65 Hz pulse rate).

states by photoexcited holes. This occurs on the sub-μs timescale, as the bleach state is observed from the start of our measurement (10 μs; Fig. 5a). The nature of this bleach state will be discussed in more detail in the next Section. In Fig. 7, for the heterojunction samples, we see a bi-phasic decay at 550 nm, which shows a power-law decay component from 10μs to $\sim$1 ms, and a long-lived exponent decay component from $\sim$1 ms to 1 s. As bulk recombination in WO_3 is known to occur on the sub-μs timescale,[57] the initial power-law decay is ascribed to the portion of holes formed in TiO_2 that were unable to transfer across the heterojunction interface that recombined with co-generated electrons.[58] This assignment is further supported by the fact that at higher TiO_2 coating thickness ($\geq$ 60 nm), the decay component increases. This is attributed to the short mean free path of holes in TiO_2,[62] which thereby limits hole transfer to WO_3 when coating thickness is increased above a threshold ($\sim$30 nm herein). This understanding is further supported by the fact that the bleach signal, due to the trapping of hole carriers in W^{5+} states, becomes obscured at TiO_2 coating thicknesses $\geq$ 60 nm.

3.5 Impact of Defects in Charge Transport Properties

Herein, our theoretical studies have only considered pristine TiO_2 and WO_3 structures form the WT heterojunction, however XPS characterization of our samples revealed the presence of a small amount of reduced tungsten species (W^{5+}).[59] In the context of electronic carrier transport in WO_3, W^{5+}-centers are treated as small electron polarons, where the self-trapped electrons in W^{5+} are facilitated by doubly ionized oxygen vacancies (V_o^{2+}) given by[57]

$$W^{6+} + V_o^{2+} + 2e^- + \frac{1}{2}O_2(g) = W^{5+} + V_o^{2+} + \frac{1}{2}O_2(g),$$

where,

$$V_o^{2+} + 2e^- + \frac{1}{2}O_2(g) \rightleftharpoons 0.$$

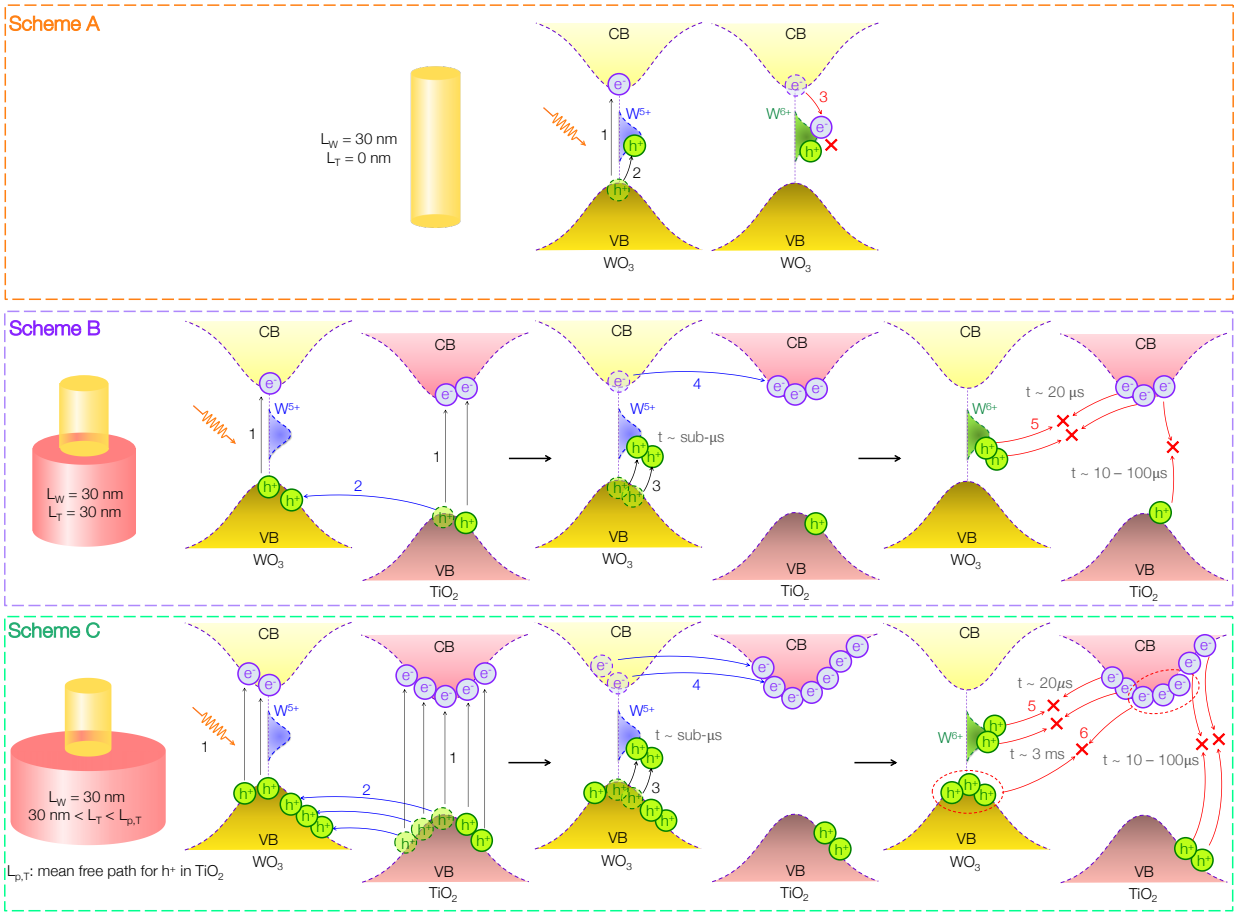

Figure 8: Proposed charge transport mechanism in WO_3 (Scheme A), WT with $L_W = 30$ nm & $L_T = 30$ nm (Scheme B) and WT with $L_W = 30$ nm & 30 nm $< L_T < L_{p,T}$ (Scheme C), with the presence of a small amount of reduced tungsten species (W^{5+}-centers).

Energetically, these trapped electrons in W^{5+} can be located in the vicinity of oxygen vacancies (thus forming electron polarons) or they can move to the conduction band *via* energetic activation (*e.g.*, thermal activation) until they are relaxed and re-trapped (*i.e.*, carrier self-trapping by polaronic states).[44,57,63,64] This is outlined for WO_3 in Scheme A, Fig. 8. Upon UV illumination (excitation energy $\leq$ E_G), the photoexcitation of electrons into the conduction band is a fast process (Step 1, Scheme A), forming photogenerated holes in the valence band (VB). These holes may be subsequently captured by the ground state polaronic W^{5+}-centers populated by the self-trapped electrons, producing W^{6+} (Step 2, Scheme A: $W^{5+} + h^+ \rightarrow W^{6+}$). According to Sachs *et al.*,[57] this dynamic process, occurs at a fast time scale of $\sim$ 100 ps–200 ps, until the electrons in the conduction band are self-captured by W^{6+} species that re-produce W^{5+}-centers (Step 3, Scheme A) and finally, WO_3 relaxes to its equilibrium condition. It is worth noting that all these processes happen at a timescale ($\geq$ 200 ps) much faster than the timescale of our study and hence, this characteristic bleaching of ground states polaronic electrons is not visible from our TAS analysis of WO_3 alone (Fig. S4).

However, the formation of the WT junction ($L_T > 0$) results in drastically altered charge transport routes, acting upon the charge transport processes occurring in the individual constituent materials of the junction. Scheme B (Fig. 8) shows the electronic implications expected upon deposition of a 30 nm TiO_2 coating (L_T = 30 nm) on our WO_3 substrate. As depicted by Step 1 (Scheme B), electron-hole pairs are generated in both WO_3 and TiO_2 in accordance to the light penetration profile shown in Fig. S3. Consequently, the WO_3 side of the junction exhibits an increased amount of photogenerated holes due to photoexcitation (Step 1, Scheme B) and a dominant thermionic emission of holes from TiO_2 to WO_3 (Step 2, Scheme B), as discussed in Fig. 4 (*vide supra*). The holes that are transferred to (or photogenerated in) WO_3 remain in WO_3 as they cannot cross the large heterojunction barrier of $\sim$0.55 eV. Nevertheless, these holes can be captured by polaronic electrons in W^{5+}-centers (Step 3, Scheme B) and contribute to the bleaching of these ground state

electrons. However, the photogenerated electrons in WO_3 can transfer to the TiO_2 side *via* Step 4 (Scheme B) – an energetically favorable conduction band process, which is facilitated by band-flattening and determined by the diffusion component of electron currents, as discussed in Fig. 4 (*vide supra*). Thus, the electrons in WO_3 are able to transfer to the TiO_2 side and avoid rapid recombination with the photogenerated holes, which are captured by the W^{5+}-centers *via* Step 3 of Scheme B. The ultimate outcome of these dynamic processes preferentially allows photogenerated holes and electrons to respectively stay in WO_3 and TiO_2, separated by the abrupt junction interface. This, in turn, is detected through our TAS measurements in terms of improved lifetimes (slowed recombination) and populations (increased ΔA) of photogenerated electrons and holes. Interestingly, as the holes captured by the W^{5+}-centers can avoid the rapid recombination with the conduction band electrons in WO_3, the bleaching of the ground state electrons in W^{5+}-centers (*via* Step 3, Scheme B) is now visible within a timescale (< 20 μs) deployed in our study (see Figs. 5a, 7b). This is a massive increase in the hole lifetime, by several orders of magnitude or more, is made possible through the formation of this unique junction with staggered valence bands. Nevertheless, at a timescale > 20 μs, holes in W^{5+}-states recombine with the adjacent electrons on the TiO_2 side of the junction (Step 5, Scheme B). As a result, the bleaching signal disappears from transient absorption spectra obtained 20 μs after UV excitation. We note that the modified recombination of electrons and holes, sitting on adjacent 'notch'-like potential distributions (shown in Fig. 4), is a hallmark characteristic of isotype abrupt heterojunctions (*e.g.*, the WT junction) and has been extensively studied by the solid-state device community.[9–11] Furthermore, in the context of photocatalytic semiconductor junctions, this engineered recombination process (Step 5, Scheme B) between holes in WO_3 and electrons in TiO_2, occurring at a comparatively slow timescale (> 20 μs), arises due to the newly introduced recombination pathways within such a heterojunction, as discussed in recent literature.[7,20]

Finally, it is important to note that the junction starts to absorb a larger portion of

the incident UV excitation, particularly in TiO_2, as the TiO_2 coating increases in thickness (*e.g.*, L_T = 60 nm, 100 nm). This is visible from the light absorption and penetration (estimated as α^{-1}, where α is the absorption coefficient) profiles in Fig. S3. In addition, the WT junctions can harness a higher number of photogenerated carriers as L_T increases. For example, the volumetric ratio between WO_3 (core) and TiO_2 (shell) increases from 1:3 to 1:8 when L_T is increased from 30 nm to 60 nm. Nevertheless, by increasing L_T, the physical location of the junction simultaneously moves further away from the surface of the WT photocatalyst, and thus progressively makes it difficult for electrons in TiO_2 to reach the surface. Concurrently, with increasing thickness photogenerated holes in TiO_2 become more prone to small polaron formation in TiO_2 *via* a self-trapping process (rather than transferring to WO_3).[60,65,66] When a large number of holes in TiO_2 start to form hole polarons, the hole transfer from TiO_2 to WO_3 will be reduced. Therefore, the optimal TiO_2 coating should be dictated by the mean free path for TiO_2 holes ($L_{p,T}$) before forming a hole polaron. Consequently, an optimal coating, larger than 30 nm and smaller than $L_{p,T}$, should thus provide optimal photocatalytic performance. Scheme C in Fig. 8 outlines the relevant process in this optimal coating regime ($L_T < L_{p,T}$). In this case, the WT junction harvests large numbers of photogenerated electrons and holes (Step 1, Scheme C). Similar to Scheme B, holes that are either generated in WO_3 or in TiO_2 in the vicinity of the junction are accumulated in WO_3 (Step 2, Scheme C). In this case, a portion of the accumulated holes in WO_3 are captured by the small amount of W^{5+}-centers (Step 3, Scheme C) and thus contribute to the bleaching of the ground state electrons in W^{5+}-centers. Concurrently, the heterojunction effectively spatially separates holes and electrons that respectively accumulate in the valence band of WO_3 and conduction band of TiO_2 (Step 4, Scheme C). These long-lived holes and electrons recombine at a timescale ∼3 ms (Step 6, Scheme C), and thereby provide a dominant positive absorption feature (Δ A > 0) throughout the spectral range of our TAS analysis. TAS data for $L_T = 60\ nm$ (Fig. 7c) and L_T = 100 nm (Fig. 7d) follow this scheme, where L_T = 60 nm provides an effective separation of photogenerated electrons and holes (long-lived carriers)

compared to the WT junction with L_T = 100 nm (the physical location of the junction being further within the TiO_2 surface and the TiO_2 side progressively becomes prone to hole polaron formation).

In summary, we combined device theory calculations and experimental TAS measurements to understand the origins of the record-efficiency (for the oxidation of stearic acid) arising from core-shell nanostructured WO_3/TiO_2 heterojunction photocatalysts. Our computational results show that photogenerated holes transferred from TiO_2 to WO_3 *via* a dominant thermionic emission process. Additionally, the holes generated in and transferred to WO_3 remain therein due to the large potential energy barrier for charge transfer ($\sim$0.55 eV) created by staggered valance band edges. Conversely, photogenerated electrons diffusively transfer from WO_3 to TiO_2 under the influence of a band flattening process, brought about by UV excitation. Micro- to milli-second (μs–ms) time-resolved measurements of photogenerated carriers were obtained using transient absorption spectroscopy. Within our WT heterojunction (L_W = 30 nm; L_T = 30 nm) accumulated holes in WO_3 depopulated W^{5+} polaronic states on the micro-second timescale ($\sim$20 μs); orders of magnitude slower than WO_3 alone (100 ps – 200 ps). Importantly, a systematic study of WT junctions (L_W = 30 nm), with differing TiO_2 layer thickness (3 nm $\leq$ L_T $\leq$ 100 nm), shows that once an optimal thickness is reached (L_T $\geq$ 30 nm), the junction can spatially separate a larger number of photogenerated electrons and holes (with respect to the parent materials), and prolong their lifetime for several hundred milli-seconds. We propose that these long-lived photogenerated carriers, spatially separated by the WT junction, can more effectively participate in the photocatalytic oxidation of stearic acid.

Overall, we believe that the combined theoretical and experimental approach, followed herein, can be used as a model to study charge carrier behavior in many other heterojunction photocatalyst systems. This strategy can help formulate materials design rules, and better facilitate the engineering and optimization of promising heterojunction systems for applications in solar fuel generation and environmental remediation.

Acknowledgement

The authors would like to acknowledge financial support from the EPSRC grant EP/R034540/1 for JSPS-EPSRC-McGill University collaboration on "Defect Functionalized Sustainable Energy Materials: From Design to Devices Application", and UCL for travel support. A. I. and K. B. thank Mitacs Globalink Research Award, NSERC of Canada and FQRNT of Québec for the financial support and the Canadian Foundation for Innovation, CalculQuebec and Compute-Canada for the computational resources provided. A. K. thanks Imperial College for a Junior Research Fellowship, the EPSRC for a Capital Award Emphasising Support for Early Career Researchers, the Royal Society for an Equipment Grant (RSG\ R1\180434), and the Grantham Institute and Energy Futures Lab for a pump priming award.

Supporting Information Available

The SI includes material parameters used in numerical computations, calculated electric field as well as experimental SEM, TEM, absorptance and TAS spectra.

This material is available free of charge via the Internet at `http://pubs.acs.org/`.

References

(1) Moniz, S. J. A.; Shevlin, S. A.; Martin, D. J.; Guo, Z.-X.; Tang, J. Visible-light driven heterojunction photocatalysts for water splitting –a critical review. Energy & Environmental Science **2015**, 8, 731–759.

(2) Wang, H.; Zhang, L.; Chen, Z.; Hu, J.; Li, S.; Wang, Z.; Liu, J.; Wang, X. Semiconductor heterojunction photocatalysts: design, construction, and photocatalytic performances. Chem. Soc. Rev. **2014**, 43, 5234–5244.

(3) Ameri, T.; Dennler, G.; Lungenschmied, C.; Brabec, C. J. Organic tandem solar cells: A review. Energy Environ. Sci. **2009**, 2, 347–363.

(4) Bach, U.; Tachibana, Y.; Moser, J.-E.; Haque, S. A.; Durrant, J. R.; Grätzel, M.; Klug, D. R. Charge Separation in Solid-State Dye-Sensitized Heterojunction Solar Cells. Journal of the American Chemical Society **1999**, 121, 7445–7446.

(5) Marschall, R. Semiconductor Composites: Strategies for Enhancing Charge Carrier Separation to Improve Photocatalytic Activity. Advanced Functional Materials **2014**, 24, 2421–2440.

(6) Stolterfoht, M.; Wolff, C. M.; Márquez, J.; Zhang, S.; Hages, C. J.; Rothhardt, D.; Albrecht, S.; Burn, P. L.; Meredith, P.; Unold, T.; Neher, D. Visualization and suppression of interfacial recombination for high-efficiency large-area pin perovskite solar cells. Nature Energy **2018**, 3, 847–854.

(7) Grigioni, I.; Stamplecoskie, K. G.; Selli, E.; Kamat, P. V. Dynamics of Photogenerated Charge Carriers in WO3/BiVO4 Heterojunction Photoanodes. The Journal of Physical Chemistry C **2015**, 119, 20792–20800.

(8) Avasthi, S.; Lee, S.; Loo, Y.-L.; Sturm, J. C. Role of Majority and Minority Carrier Barriers Silicon/Organic Hybrid Heterojunction Solar Cells. Advanced Materials **2011**, 23, 5762–5766.

(9) Kroemer, H.; Griffiths, G. Staggered-lineup heterojunctions as sources of tunable below-gap radiation: Operating principle and semiconductor selection. IEEE Electron Device Letters **1983**, 4, 20–22.

(10) Oldham, W. G.; Milnes, A. G. n-n Semiconductor heterojunctions. Solid-State Electronics **1963**, 6, 121–132.

(11) Sze, S.; Kwok, K. N. Physics of Semiconductor Devices; John Wiley & Sons, Ltd, 2006.

(12) Ohtomo, A.; Hwang, H. Y. A high-mobility electron gas at the LaAlO3/SrTiO3 heterointerface. Nature **2004**, 427, 423–426.

(13) Geim, A. K.; Grigorieva, I. V. Van der Waals heterostructures. Nature **2013**, 499, 419–425.

(14) De Wolf, S.; Descoeudres, A.; Holman, Z. C.; Ballif, C. High-efficiency Silicon Heterojunction Solar Cells: A Review. Green **2012**, 2, 7–24.

(15) Vithanage, D. A.; Devižis, A.; Abramavičius, V.; Infahsaeng, Y.; Abramavičius, D.; MacKenzie, R. C. I.; Keivanidis, P. E.; Yartsev, A.; Hertel, D.; Nelson, J.; Sundström, V.; Gulbinas, V. Visualizing charge separation in bulk heterojunction organic solar cells. Nature Communications **2013**, 4, 2334.

(16) Degler, D.; Weimar, U.; Barsan, N. Current Understanding of the Fundamental Mechanisms of Doped and Loaded Semiconducting Metal-Oxide-Based Gas Sensing Materials. ACS Sensors **2019**, 4, 2228–2249.

(17) Miller, D. R.; Akbar, S. A.; Morris, P. A. Nanoscale metal oxide-based heterojunctions for gas sensing: A review. Sensors and Actuators B: Chemical **2014**, 204, 250–272.

(18) Selim, S.; Francàs, L.; García-Tecedor, M.; Corby, S.; Blackman, C.; Gimenez, S.; Durrant, J. R.; Kafizas, A. WO_3/$BiVO_4$: impact of charge separation at the timescale of water oxidation. Chemical Science **2019**, 10, 2643–2652.

(19) Su, J.; Guo, L.; Bao, N.; Grimes, C. A. Nanostructured WO3/BiVO4 Heterojunction Films for Efficient Photoelectrochemical Water Splitting. Nano Letters **2011**, 11, 1928–1933.

(20) Grigioni, I.; Stamplecoskie, K. G.; Jara, D. H.; Dozzi, M. V.; Oriana, A.; Cerullo, G.; Kamat, P. V.; Selli, E. Wavelength-Dependent Ultrafast Charge Carrier Separation in the WO3/BiVO4 Coupled System. ACS Energy Letters **2017**, 2, 1362–1367.

(21) Sotelo-Vazquez, C.; Quesada-Cabrera, R.; Ling, M.; Scanlon, D. O.; Kafizas, A.; Thakur, P. K.; Lee, T.-L.; Taylor, A.; Watson, G. W.; Palgrave, R. G.; Durrant, J. R.; Blackman, C. S.; Parkin, I. P. Evidence and Effect of Photogenerated Charge Transfer for Enhanced Photocatalysis in WO_3/TiO_2 Heterojunction Films: A Computational and Experimental Study. Advanced Functional Materials **2017**, 27, 1605413.

(22) Higashimoto, S.; Sakiyama, M.; Azuma, M. Photoelectrochemical properties of hybrid WO3/TiO2 electrode. Effect of structures of WO3 on charge separation behavior. Thin Solid Films **2006**, 503, 201–206.

(23) Smith, W.; Wolcott, A.; Fitzmorris, R. C.; Zhang, J. Z.; Zhao, Y. Quasi-core-shell TiO2/WO3 and WO3/TiO2 nanorod arrays fabricated by glancing angle deposition for solar water splitting. Journal of Materials Chemistry **2011**, 21, 10792–10800.

(24) Moniz, S. J. A.; Zhu, J.; Tang, J. 1D Co-Pi Modified BiVO4/ZnO Junction Cascade for Efficient Photoelectrochemical Water Cleavage. Advanced Energy Materials **2014**, 4, 1301590.

(25) Mi, Z., Wang, L., Jagadish, C., Eds. Semiconductors for Photocatalysis; Semiconductors and Semimetals; Academic Press, 2017; Vol. 97.

(26) Low, J.; Yu., J.; Jaroniec, M.; Wageh, S.; Al-Ghamdi, A. A. Heterojunction Photocatalysts. Advanced Materials **2017**, 29, 1601694.

(27) Mondal, K.; Sharma, A. Recent advances in the synthesis and application of photocatalytic metal–metal oxide core–shell nanoparticles for environmental remediation and their recycling process. RSC Advances **2016**, 6, 83589–83612.

(28) Xu, Q.; Zhang, L.; Cheng, B.; Fan, J.; Yu, J. S-Scheme Heterojunction Photocatalyst. Chem **2020**, 6, 1543–1559.

(29) Zhang, J.; Liu, Z.; Liu, Z. Novel WO3/Sb2S3 Heterojunction Photocatalyst Based on WO3 of Different Morphologies for Enhanced Efficiency in Photoelectrochemical Water Splitting. ACS Applied Materials & Interfaces **2016**, 8, 9684–9691.

(30) Paracchino, A.; Laporte, V.; Sivula, K.; Grätzel, M.; Thimsen, E. Highly active oxide photocathode for photoelectrochemical water reduction. Nature Materials **2011**, 10, 456–461.

(31) Gardecka, A. J.; Bishop, C.; Lee, D.; Corby, S.; Parkin, I. P.; Kafizas, A.; Krumdieck, S. High efficiency water splitting photoanodes composed of nano-structured anatase-rutile TiO2 heterojunctions by pulsed-pressure MOCVD. Applied Catalysis B: Environmental **2018**, 224, 904–911.

(32) Kafizas, A.; Wang, X.; Pendlebury, S. R.; Barnes, P.; Ling, M.; Sotelo-Vazquez, C.; Quesada-Cabrera, R.; Li, C.; Parkin, I. P.; Durrant, J. R. Where Do Photogenerated Holes Go in Anatase:Rutile TiO_2? A Transient Absorption Spectroscopy Study of Charge Transfer and Lifetime. The Journal of Physical Chemistry A **2016**, 120, 715–723.

(33) Scanlon, D. O.; Dunnill, C. W.; Buckeridge, J.; Shevlin, S. A.; Logsdail, A. J.; Woodley, S. M.; Catlow, C. R. A.; Powell, M. J.; Palgrave, R. G.; Parkin, I. P.; Watson, G. W.; Keal, T. W.; Sherwood, P.; Walsh, A.; Sokol, A. A. Band alignment of rutile and anatase TiO2. Nature Materials **2013**, 12, 798–801.

(34) Abazović, N. D.; Čomor, M. I.; Dramićanin, M. D.; Jovanović, D. J.; Ahrenkiel, S. P.; Nedeljković, J. M. Photoluminescence of Anatase and Rutile TiO2 Particles. The Journal of Physical Chemistry B **2006**, 110, 25366–25370.

(35) Xiong, G.; Shao, R.; Droubay, T.; Joly, A.; Beck, K.; Chambers, S.; Hess, W. Photoemission Electron Microscopy of TiO2 Anatase Films Embedded with Rutile Nanocrystals. Advanced Functional Materials **2007**, 17, 2133–2138.

(36) Ràfols i Bellés, C.; Selim, S.; Harrison, N. M.; Ahmad, E. A.; Kafizas, A. Beyond band bending in the WO3/BiVO4 heterojunction: insight from DFT and experiment. Sustainable Energy & Fuels **2019**, 3, 264–271.

(37) Zhou, B.-X.; Huang, W.-Q.; Yang, K.; Ding, S.; Xie, Z.; Pan, A.; Hu, W.; Peng, P.; Huang, G.-F. Theory-Driven Heterojunction Photocatalyst Design with Continuously Adjustable Band Gap Materials. The Journal of Physical Chemistry C **2018**, 122, 28065–28074.

(38) Xue, J.; Fujitsuka, M.; Majima, T. Shallow Trap State-Induced Efficient Electron Transfer at the Interface of Heterojunction Photocatalysts: The Crucial Role of Vacancy Defects. ACS Applied Materials & Interfaces **2019**, 11, 40860–40867.

(39) Zhang, J.; Liu, Z.; Liu, Z. Novel WO3/Sb2S3 Heterojunction Photocatalyst Based on WO3 of Different Morphologies for Enhanced Efficiency in Photoelectrochemical Water Splitting. ACS Applied Materials & Interfaces **2016**, 8, 9684–9691.

(40) Chen, Z.; Xu, Y.-J. Ultrathin TiO2 Layer Coated-CdS Spheres Core–Shell Nanocomposite with Enhanced Visible-Light Photoactivity. ACS Applied Materials & Interfaces **2013**, 5, 13353–13363.

(41) Ge, H.; Xu, F.; Cheng, B.; Yu, J.; Ho, W. S-Scheme Heterojunction TiO2/CdS Nanocomposite Nanofiber as H2-Production Photocatalyst. ChemCatChem **2019**, 11, 6301–6309.

(42) Xu, F.; Meng, K.; Cheng, B.; Wang, S.; Xu, J.; Yu, J. Unique S-scheme heterojunctions in self-assembled TiO2/CsPbBr3 hybrids for CO2 photoreduction. Nature Communications **2020**, 11, 4613.

(43) Florica, C.; Costas, A.; Preda, N.; Beregoi, M.; Kuncser, A.; Apostol, N.; Popa, C.; Socol, G.; Diculescu, V.; Enculescu, I. Core-shell nanowire arrays based on ZnO and CuxO for water stable photocatalysts. Scientific Reports **2019**, 9, 17268.

(44) Pastor, E.; Park, J.-S.; Steier, L.; Kim, S.; Grätzel, M.; Durrant, J. R.; Walsh, A.; Bakulin, A. A. In situ observation of picosecond polaron self-localisation in Îś-Fe2O3 photoelectrochemical cells. Nature Communications **2019**, 10, 3962.

(45) Wiktor, J.; Ambrosio, F.; Pasquarello, A. Role of Polarons in Water Splitting: The Case of BiVO4. ACS Energy Letters **2018**, 3, 1693–1697.

(46) Ling, M.; Blackman, C. Growth mechanism of planar or nanorod structured tungsten oxide thin films deposited via aerosol assisted chemical vapour deposition (AACVD). physica status solidi c **2015**, 12, 869–877.

(47) Iqbal, A.; Bevan, K. H. Simultaneously Solving the Photovoltage and Photocurrent at Semiconductor–Liquid Interfaces. Journal of Physical Chemistry C **2018**, 122, 30–43.

(48) Iqbal, A.; Bevan, K. H. The impact of boundary conditions on calculated photovoltages and photocurrents at photocatalytic interfaces. MRS Communications **2018**, 1–8.

(49) Iqbal, A.; Yuan, S.; Wang, Z.; Bevan, K. H. Impact of Bulk Trapping Phenomena on the Maximum Attainable Photovoltage of Semiconductor–Liquid Interfaces. The Journal of Physical Chemistry C **2018**, 122, 23878–23889.

(50) Selberherr, S. Analysis and simulation of semiconductor devices; Springer-Verlag Wien New York, 1984.

(51) Chang, L. L. The conduction properties of Ge–$GaAs_{1x}P_x$ nâĹŠn heterojunctions. Solid-State Electronics **1965**, 8, 721–728.

(52) Pesci, F. M.; Cowan, A. J.; Alexander, B. D.; Durrant, J. R.; Klug, D. R. Charge Carrier Dynamics on Mesoporous WO3 during Water Splitting. Journal of Physical Chemistry Letters **2011**, 2, 1900–1903.

(53) Corby, S.; Pastor, E.; Dong, Y.; Zheng, X.; Francàs, L.; Sachs, M.; Selim, S.; Kafizas, A.;

Bakulin, A. A.; Durrant, J. R. Charge Separation, Band-Bending, and Recombination in WO3 Photoanodes. The Journal of Physical Chemistry Letters **2019**, 10, 5395–5401.

(54) Jang, J.; Du, C.; Ye, Y.; Lin, Y.; Yao, X.; Thorne, J. E.; Liu, E.; McMahon, G.; Zhu, J.; Javey, A.; Guo, J.; Wang, D. Enabling Unassisted Solar Water Splitting by Iron Oxide and Silicon. Nature Communications **2015**, 6, 7447.

(55) Yang, K.; East, J. R.; Haddad, G. I. Numerical modeling of abrupt heterojunctions using a thermionic-field emission boundary condition. Solid-State Electronics **1993**, 36, 321–330.

(56) Moss, B.; Lim, K. K.; Beltram, A.; Moniz, S.; Tang, J.; Fornasiero, P.; Barnes, P.; Durrant, J.; Kafizas, A. Comparing photoelectrochemical water oxidation, recombination kinetics and charge trapping in the three polymorphs of TiO2. Scientific Reports **2017**, 7, 2938.

(57) Sachs, M.; Park, J.-S.; Pastor, E.; Kafizas, A.; Wilson, A. A.; Francàs, L.; Gul, S.; Ling, M.; Blackman, C.; Yano, J.; Walsh, A.; Durrant, J. R. Effect of oxygen deficiency on the excited state kinetics of WO3 and implications for photocatalysis. Chem. Sci. **2019**, 10, 5667–5677.

(58) Wang, X.; Kafizas, A.; Li, X.; Moniz, S. J. A.; Reardon, P. J. T.; Tang, J.; Parkin, I. P.; Durrant, J. R. Transient Absorption Spectroscopy of Anatase and Rutile: The Impact of Morphology and Phase on Photocatalytic Activity. Journal of Physical Chemistry C **2015**, 119, 10439–10447.

(59) Nunzi, F.; De Angelis, F.; Selloni, A. Ab Initio Simulation of the Absorption Spectra of Photoexcited Carriers in TiO2 Nanoparticles. The Journal of Physical Chemistry Letters **2016**, 7, 3597–3602.

(60) Zawadzki, P. Absorption Spectra of Trapped Holes in Anatase TiO2. The Journal of Physical Chemistry C **2013**, 117, 8647–8651.

(61) Wiktor, J.; Ambrosio, F.; Pasquarello, A. Role of Polarons in Water Splitting: The Case of BiVO4. ACS Energy Letters **2018**, 3, 1693–1697.

(62) Salvador, P. Hole diffusion length in nâĂŘTiO_2 single crystals and sintered electrodes: Photoelectrochemical determination and comparative analysis. Journal of Applied Physics **1984**, 55, 2977.

(63) Chatman, S.; Pearce, C. I.; Rosso, K. M. Charge Transport at Ti-Doped Hematite (001)/Aqeuous Interfaces. Chemistry of Materials **2015**, 27, 1665–1673.

(64) Wang, Z.; Brock, C.; Matt, A.; Bevan, K. H. Implications of the DFT+U method on polaron properties in energy materials. Physical Review B **2017**, 96, 125150–.

(65) Zawadzki, P.; Jacobsen, K. W.; Rossmeisl, J. Electronic hole localization in rutile and anatase TiO2 –Self-interaction correction in ÎŤ-SCF DFT. Chemical Physics Letters **2011**, 506, 42–45.

(66) Tamaki, Y.; Furube, A.; Murai, M.; Hara, K.; Katoh, R.; Tachiya, M. Direct Observation of Reactive Trapped Holes in TiO2 Undergoing Photocatalytic Oxidation of Adsorbed Alcohols: Evaluation of the Reaction Rates and Yields. Journal of the American Chemical Society **2006**, 128, 416–417.

Graphical TOC Entry